# Internal Conversion and Intersystem Crossing Dynamics based on Coupled Potential Energy Surfaces with full geometry-dependent spin-orbit and derivative couplings. Nonadiabatic photodissociation dynamics of NH3(A) leading to the NH(X3Σ-, a1Δ,) + H2 channel.

| | |
|---|---|
| Journal: | *Physical Chemistry Chemical Physics* |
| Manuscript ID | CP-ART-03-2022-001271.R1 |
| Article Type: | Paper |
| Date Submitted by the Author: | 26-May-2022 |
| Complete List of Authors: | Wang, Yuchen; Johns Hopkins University - Homewood Campus, Chemistry<br>Guo, Hua; University of New Mexico, Department of Chemistry<br>Yarkony, David; Johns Hopkins University, Department of Chemistry |
| | |

# Internal Conversion and Intersystem Crossing Dynamics Based on Coupled Potential Energy Surfaces with Full Geometry-Dependent Spin-Orbit and Derivative Couplings. Nonadiabatic Photodissociation Dynamics of $NH_3(\tilde{A})$ Leading to the $NH(X^3\Sigma^-, a^1\Delta) + H_2$ Channel

Yuchen Wang,[a,*] Hua Guo,[b] and David R. Yarkony[a]

[a]Department of Chemistry, Johns Hopkins University, Baltimore, Maryland 21218, USA

[b]Department of Chemistry and Chemical Biology, University of New Mexico, Albuquerque, New Mexico 87131, USA

*: corresponding author: Yuchen Wang: ywang312@jhu.edu

## Abstract

We simulate the photodissociation of $NH_3$ originating from its first excited singlet state $S_1$ into the $NH_2$+H (radical) and NH+$H_2$ (molecular) channels. The states considered are the ground singlet state $S_0$, the first excited singlet state $S_1$ and the lowest-lying triplet state $T_1$, which permit for the first time a uniform treatment of the internal conversion and intersystem crossing. The simulations are based on a diabatic potential energy matrix (DPEM) of $S_0$, $S_1$ coupled by a conical intersection seam, as well as a potential energy surface (PES) for $T_1$ coupled by spin-orbit coupling (SOC) to the two singlet states. The DPEM and PES are fitted to *ab initio* electronic structure data (ESD) including energies, energy gradients, and derivative couplings. The DPEM also defines an adiabatic to diabatic state (AtD) transformation, which is used to transform the singular adiabatic SOC into a smooth function of the nuclear coordinates in the diabatic representation, allowing the diabatic SOC to be fit to an analytical functional form. ESD and SOC data obtained from these surfaces can serve as input for either quantum or semi-classical characterization of the nonadiabatic dynamics. Using the SHARC suite of programs, nonadiabatic simulations based on over 40,000 semi-classical trajectories assess the convergence of our results. The production of NH+$H_2$ is not direct, but is only achieved through a quasi-statistical dissociation mechanism after internal conversion to the ground electronic state. This leads to a much lower yield comparing with the main $NH_2$+H channel. The NH($X^3\Sigma^-$) radical produced through the intersystem crossing from $S_0$ to $T_1$ is rare (~0.2%) compared to NH($a^1\Delta$) due to the process being spin forbidden.

## I. Introduction

Nonadiabatic processes involve nuclear motion on more than one potential energy surface (PES).[1-4] Such processes are ubiquitous in nature and understanding them requires quality simulation methods.[5-14] In this work, we focus on the first principle determination of the molecular product channel of the nonadiabatic photodissociation

$$NH_3(1^1A) \xrightarrow{hv} NH_3(2^1A) \rightarrow NH_2(X,A) + H \qquad \text{(radical channel)} \qquad (1a)$$

$$\rightarrow NH(X^3\Sigma^-, a^1\Delta) + H_2. \qquad \text{(molecular channel)} \qquad (1b)$$

Internal conversion (1a) and intersystem crossing (1b) are the two major mechanisms of nonradiative decay, with the former involving states with same spin multiplicity and induced by conical intersections and the latter involving states with different spin multiplicities and induced by spin-orbit coupling (SOC).[15-17] Recently, there has been significant interest in competition between these two mechanisms.[7, 18-24] In a previous work, we reported analytical surfaces of the diabatic potential energy matrix (DPEM) for the singlet manifold, the potential energy surface (PES) for the triplet state and their SOC interactions obtained from accurate electronic structure data (ESD).[25] The surfaces were combined to give a comprehensive description of reactions (1a) and (1b). In this follow-up work, we report nonadiabatic semi-classical simulation results based on previously reported surfaces with particular attention paid to reaction (1b) as it potentially exhibits both internal conversion and intersystem crossing, with complex formation making up for weak spin-orbit coupling, in the latter case.

There are two complementary ways to carry out nonadiabatic molecular dynamics calculations: (i) "on-the-fly" methods where ESD are produced by explicit computation at each time step during the simulation of the nuclear dynamics[6, 7, 26] and (ii) fit-surface methods[8, 27, 28] where requisite ESD (herein energies, energy gradients, and derivative couplings) are encoded in smooth functions of nuclear coordinates in a diabatic representation whose determination is a key aspect of the simulation. An advantage of the on-the-fly approach is that it can calculate any additional matrix elements (here SOCs) not required for the standard Coulomb Hamiltonian as the electronic wave functions are available at each point. However, on-the-fly approach is limited by the time to completion of ESD calculations, which precludes their use with advanced, high-level electronic structure descriptions. The fit-surface method provides ESD in negligible time during simulations, enabling full quantum nuclear dynamics. For trajectory surface hopping (TSH) simulations, it can sustain larger ensembles of trajectories for longer propagation times with the latter attribute being essential for nonradiative decay induced by SOC. Recently, we have reported methods to construct dipole and SOC surfaces in nonadiabatic systems, allowing fit-surface methods to compete with on-the-fly methods in simulating SOC induced nonadiabatic transitions.[25, 29, 30] When SOC is small, the fit-surface methods are particularly advantageous as nonadiabatic transitions are rare events that requires a large number of trajectories to achieve reasonable statistics. The principal disadvantage is that the construction of high-quality DPEMs is challenging, especially when it comes to high-dimensional systems.

The photodissociation of $NH_3$ has been extensively studied by experiment and theory.[31-50] Experimental measurements have identified $NH_2$+H (1a) as the major dissociation channel, with other minor dissociation channels including NH+$H_2$ (1b)[41] and at higher energies NH+H+H[31] also being reported. Accurate coupled PESs for the radical channel[29, 51] and the molecular channel[25] have been described. The PESs are based on *ab initio* data from multi-reference configuration interaction (MRCI) wavefunctions, with which the bond breaking process can be accurately described. Here we focus on the molecular dissociation channel that produces NH+$H_2$, from $NH_3$ originating on the $S_1$ state, addressing practical and didactic issues. A high energy barrier[25] in the molecular regions makes the reaction (1b) a minor channel. The mechanism will be described in this work using semi-classical trajectories, which follow not only the internal conversion pathway to NH($a^1\Delta$), as discussed in our earlier work,[25] but also intersystem crossing pathway to NH($X^3\Sigma^-$) for the first time. The latter is particularly difficult to anticipate and energetics in the vicinity of the minimum singlet-triplet crossing will prove significant in that regard, and also present a challenge to on-the-fly methods because of its small probability. Methodologically, we will be concerned with how many trajectories are required to converge the computed product distributions, the time required to reach the product channels and the competition between internal conversion (IC) and intersystem crossing (ISC.) .

The paper is organized as follows. Section II introduces the computational treatment of quasi-diabatic Hamiltonian including SOC. In section III, the constructed electronic Hamiltonian is used to conduct TSH simulations of the photodissociation of $NH_3(2^1A)$. The results are analyzed and discussed in that section. Section IV concludes and summarizes.

## II. Computational Treatment

### A.The Spin-diabatic Electronic Hamiltonian in its Adiabatic and Diabatic Forms. A brief review

The total *electronic* Hamiltonian, is given by $\hat{H}^{tot} = \hat{H}^{sf} + \hat{H}^{so}$, where $\hat{H}^{sf}$ and $\hat{H}^{so}$ are respectively the spin-free (Coulomb + scalar relativistic contributions) nonrelativistic Hamiltonian operator and SOC operator in the Breit-Pauli approximation[15, 52]. The basis states for this operator are eigenstates of $\hat{H}^{sf}$, $\psi_{k}^{S,\ M,(a)}$ where *S* is the total electron spin, *M* is the z-component of *S*, $(a)$ is adiabatic and *k* indexes the $N^S$ nonrelativistic states with spin symmetry *S*. Note *M*, with *M* =-*S*, -*S*+1, …, *S*-1, *S*, is a good quantum number for example using a configuration state function (CSF) basis, the basis used in the *ab initio* calculations. The selection of these "frontier" basis states is a key issue in formulating the treatment. In this work we used the "canonical basis" $N^0$=2, $N^1$=1 to describe two singlets and one triplet.

In this basis, we have for $H^{sf}$

$$< \psi_k^{S,M,(a)} | \hat{H}^{sf} | \psi_{k'}^{S',M',(a)} > \; = \hat{H}^{sf,(a)}_{S,M,k;S',M',k'} = E_k^S \delta_{S,S'} \delta_{M,M'} \delta_{k,k'} \qquad (2a)$$

where $E_k^S$ are the adiabatic $(a)$ energies of $\hat{H}^{sf}$. The SOC matrix elements are defined in eq. (2b)

$$\hat{H}^{so,(a)}_{S,M,k;S',M',k'} = \; < \psi_k^{S,M,(a)} | \hat{H}^{so} | \psi_{k'}^{S',M',(a)} > \qquad (2b)$$

They are evaluated with the help of the Wigner-Eckart theorem and the work of McWeeny as discussed in refs. [53, 54]. Since there is no derivative coupling between states with different values of *S*, we will refer to this representation as an *adiabatic spin-diabatic basis*.[55] This adiabatic representation works well provided no conical intersection induced singularities are present for a given $S$. In the presence of that ubiquitous feature of coupled PESs, the SOC data will be discontinuous at the points of conical intersection and therefore not suitable for fitting by analytic functions.

In such circumstances, we use diabatized SOC data from

$$\boldsymbol{\psi}^{S,M,(d)} = \mathbf{U}^{S}\boldsymbol{\psi}^{S,M,(a)} \tag{3}$$

Here, $d$ denotes the diabatic representation, $\mathbf{U}^{S}$ is the $N^{s} \times N^{s}$ unitary adiabatic to diabatic (AtD) transformation matrix that can be extracted from DPEM. After the transformation the individual SOC matrix elements are smooth function of nuclear coordinates and can be fit with a continuous functional form. Thus $\mathbf{H}^{\mathrm{tot}}$ is a 5x5 matrix given in Table I whose off-diagonal, singlet-triplet coupling matrix elements $\hat{H}^{so,(e)}_{S,M,k;S',M',k'}$ are given by $\hat{H}^{so,(e)}_{0,0,k;1,m,1}$ = $W^{(m),(e)}_{k}$ where $W^{(m),(e)}_{k} = X^{(e)}_{k}, Y^{(e)}_{k}, Z^{(e)}_{k}$ for $m$ = -1, 1, 0 and $k$ = 0, 1, respectively.[25] $\mathbf{W}^{(\mathrm{m})(\mathrm{e})}$ are evaluated from the *ab initio* adiabatic wave functions. The $m$ labels the three time reversal adapted linear combinations of the triplet functions,[30] and $H^{(a)}_{0,0} = E_{S_0}$, $H^{(a)}_{1,1} = E_{S_1}$, $H^{(a)}_{0,1} = 0$.

Table I. $\widehat{H}^{tot}$ in Spin-diabatic basis ($\mathbf{H}^{(a)}$)

| $\hat{\boldsymbol{H}}^{\boldsymbol{tot}}$ | $\|\boldsymbol{S_0}>$ | $\|\boldsymbol{S_1}>$ | $\|\boldsymbol{T^{tr}_{-}}>$ | $\|\boldsymbol{T^{tr}_{+}}>$ | $\|\boldsymbol{T^{tr}_{0}}>$ |
|---|---|---|---|---|---|
| $<\boldsymbol{S_0}\|$ | $E_{S_0}$ | 0 | $X_0$ | $Y_0$ | $Z_0$ |
| $<\boldsymbol{S_1}\|$ | *0* | $E_{S_1}$ | $X_1$ | $Y_1$ | $Z_1$ |
| $<\boldsymbol{T^{tr}_{-}}\|$ | $X_0$ | $X_1$ | $E_{T_1}$ | 0 | 0 |
| $<\boldsymbol{T^{tr}_{+}}\|$ | $Y_0$ | $Y_1$ | 0 | $E_{T_1}$ | 0 |
| $<\boldsymbol{T^{tr}_{0}}\|$ | $Z_0$ | $Z_1$ | 0 | 0 | $E_{T_1}$ |

Simulations of nuclear dynamics can either be carried out in the adiabatic or diabatic representation. Figure 1 presents a flow sheet describing preparation of ESD for either semi-classical or quantum dynamics. Note that if adiabatic ESD is used, as in most on-the-fly molecular dynamics simulations, additional steps are needed to convert the diabatic $\widehat{H}^{tot}$ back to an adiabatic form. The real-valued SOC matrix elements in time-reversal basis are also transformed back into complex numbers using the time reversal adapted linear combinations. The two inverted transformations are used to ensure on-the-fly program uses ESD in the original adiabatic form as if they are obtained from *ab initio* calculation.

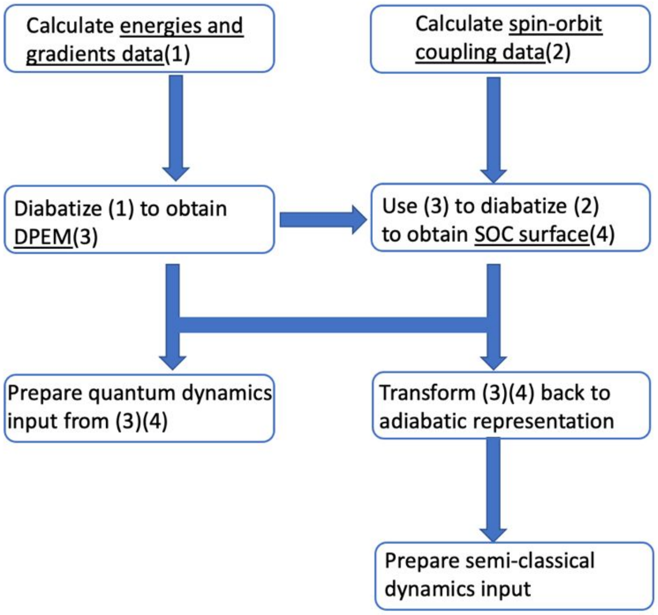

Figure 1. Diagram for constructing a DPEM including SOC data and using the DPEM for input to dynamics simulations

## B. On-the-fly vs. fit-coupled-surface dynamics

A simple estimation for the computational cost of on-the-fly method in this system is provided here. Approximate time for a single on-the-fly data point including all energies, energy gradients, derivative and spin-orbit couplings, using the highly parallelized MRCI implemented in COLUMBUS[56-58] is ~1 hour on a 24-core machine. In this work, trajectories were propagated for 1 ps and the timestep is 0.5 fs. The maximum time required for a single trajectory would then be ~2000 hours . It is beyond our current ability to compute large numbers of such trajectories. With the DPEM and SOC surfaces, the time required for ESD calculation is negligible, although note this analysis does not include the time to construct the surface fits, which may be substantial.

The ability to propagate large numbers of trajectories for long times enables the fit surface method to address issues which are not amenable to treatment using the on-the-fly approach. These issues include convergence of measureable properties including branching fractions and testing of statistical models using long time propagated trajectories. The convergence of semi-classical simulations is an important issue in nonadiabadic dynamics to which we will devote considerable resources here and in the future.

## III. $NH_3$ photodissociation in the A band

The photodissociation of $NH_3$(A) is described using a modified version of a previously reported DPEM[25, 29] based on ESD at~3000 points. To that data set ~400 points were added to provide a better description of the ($S_0/T_1$) intersection in the molecular dissociation channel and the ($S_0$, $S_1$) symmetry required energy degeneracy in the $NH+H_2$ asymptote region. All electronic structure calculations reported here are determined by COLUMBUS[56-58] and semi-classical trajectories are calculated by SHARC.[7, 14, 59]

### A. Critical points on the $NH_3$ surfaces

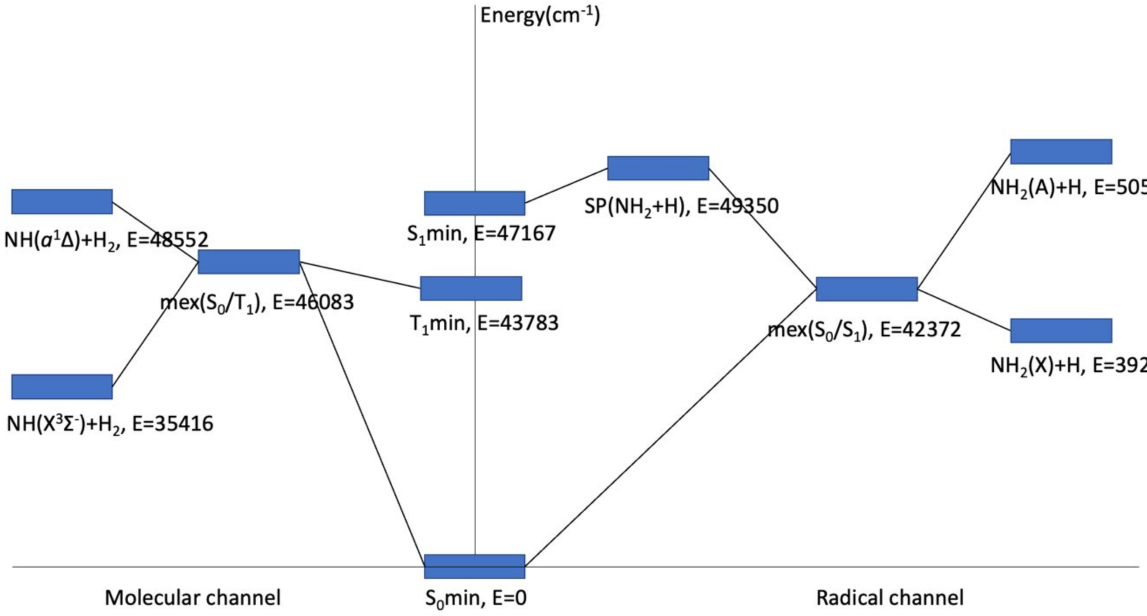

Figure 2: Reaction diagram for the two-channel dissociation of $NH_3$. The minima (min), saddle points (SP), and the minimum energy crossings (mex) are indicated in the figure.

The above figure summarizes the critical points along paths to the radical and molecular asymptotes. Most of the critical points, as well as 2D and 3D cuts of PESs are reported in ref [25]. We added the singlet-triplet crossing mex($S_0/T_1$) here. This crossing is energetically accessible considering the excitation energies and excited state minima energies. Note that in the molecular channel $S_0$ and $S_1$ become degenerate as they correlate with the doubly degenerate NH($a^1\Delta$) state. An allowed crossing between $S_0$ and $T_1$ is guaranteed along a dissociation path since the NH($X^3\Sigma^-$) state is the ground state asymptotically. We refer the reader to ref. [34] for a more detailed discussion of the state correlation diagram in molecular channel.

## B. SOC geometry dependence

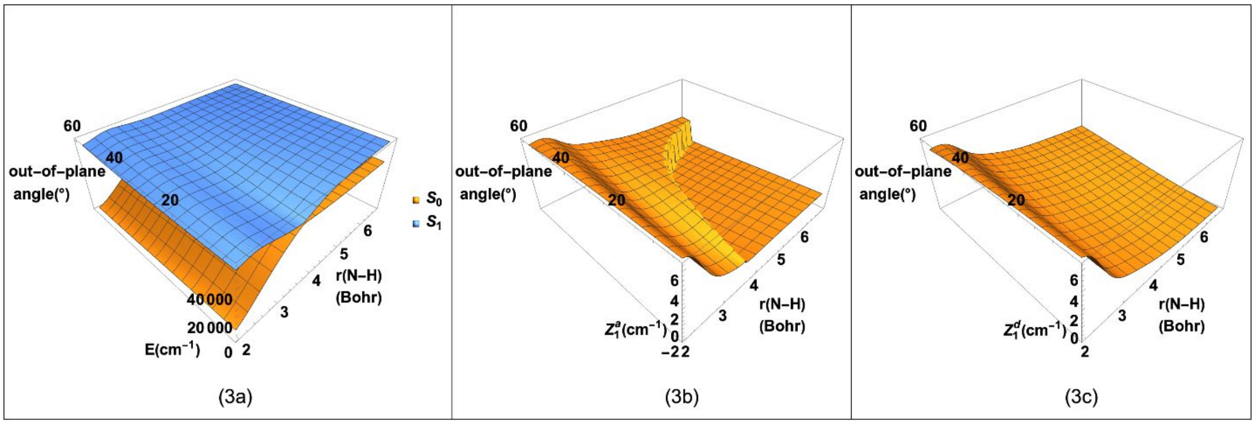

Figure 3. Surfaces in the radical channel ($NH_2$+H), (a) adiabatic PESs (b) SOC matrix element $Z_1$ shown in adiabatic basis (c) $Z_1$ in diabatic basis. $Y$-axis is the out-of-plane angle between dissociated hydrogen atom and $NH_2$ plane.

A detailed discussion of the SOC surfaces used in this work can be found in ref. [25]. Here we reproduce in Fig. 3 one dominant matrix element ($Z_1$) in both the adiabatic and diabatic representations to address the necessity of the AtD transformations. It is clear from Fig. 3a that $S_0$ and $S_1$ in the $NH_2$+H channel are coupled by a conical intersection near $R$(N-H) ~3.6 Bohr. There is the inevitable discontinuity in the adiabatic SOC near the conical intersection shown in Fig. 3b. A correct treatment requires transforming the SOC to the diabatic representation as shown in Fig. 3c, in which the wavefunction is a slowly varying function in the vicinity of a conical intersection and the SOC surfaces are then smooth. For the molecular channel (NH+$H_2$) channel, the SOC is already a largely continuous function in adiabatic basis because ($S_0$, $S_1$) conical intersections are absent in this channel.

## C. Surface hopping simulations

The trajectory surface hopping (TSH) results reported here are based on 40000 trajectories performed by SHARC.[7, 14, 59] SHARC is an *ab initio* molecular dynamics package that is capable of treating nonadiabatic couplings at conical intersections and intersystem crossing induced by SOC on an equal footing. It uses ESD in the adiabatic representation. Therefore we need to prepare SOC input in the adiabatic spin-diabatic representation described above.[See Figure 1] For this work, we interfaced SHARC with our previously reported DPEM, PES and SOC surfaces for $NH_3$ $1,2^1A$ and $1^3A$ states also denoted $S_0$, $S_1$ and $T_1$, respectively. Trajectories were begun on the $2^1A$ surface. Initial conditions were generated from a Wigner distribution determined by SHARC. A trajectory is considered finished when the distance between any atoms is greater than 10 Bohr or the simulation time limit of 1ps has been reached.

The first set of 10000 trajectories considered convergence of a single ensemble of trajectories with a range of total energy of 8.2-8.6 eV. We consider the branching into $NH_2$(X,A), NH($a$) and NH(X). In Table IIwe report the product branching percentages obtained from ensembles of increasing size in order to estimate its convergence. It is clear that for 100 random trajectories the results are not converged. Importantly, NH($X^3\Sigma^-$) is not observed, making for a large percentage error. This is not surprising as for small probability events, results are subject to significant sampling errors if a small number of trajectories are counted. From the table, a converged result requires at least 2000 trajectories, which is usually considered too expensive for on-the-fly simulations.

Table II. The product branching percentages as a function of numbers of trajectories

| Number of trajectories | $NH_2$+H | NH+$H_2$ $a^1\Delta$,($X^3\Sigma^-$) | No dissociation |
|---|---|---|---|
| 100 | 98.0% | 2.0% (0%) | 0% |
| 500 | 97.0% | 1.2% (0.4%) | 1.8% |
| 1000 | 97.1% | 1.4% (0.3%) | 1.5% |
| 2000 | 97.0% | 1.9% (0.2%) | 1.1% |
| 5000 | 97.1% | 1.8% (0.2%) | 1.1% |
| 10000 | 97.0% | 1.8% (0.2%) | 1.2% |

We examine the yield of NH+$H_2$ as a function of the total energy ($E_0^{tot}$). For each assigned $E_0^{tot}$, we select $M$ initial conditions that have total energy $E_0^{tot}$±0.05eV and run trajectory simulations with them. Taking $M$ =2500, 5000 and 7500 allows us to discuss convergence. The results are reported in Table III. Noted that even for 2500 trajectories, the yield of NH($a^1\Delta$) at lower initial energy such as 7.4 and 7.6 eV still exhibit a relatively large percentage error compared with the well-converged values at 7500 trajectories. The total trajectory number required for convergence increases when the product yield becomes lower, which is a result of the increasing difficulty in sampling small probability events. In general, 5000 trajectory is enough to converge the product yield at the magnitude of ~0.2%.

We next discuss the energy dependency of $NH+H_2$ channel. The $NH+H_2$ is a minor channel in $NH_3$ photolysis, with increasing yield at higher trajectory energies. This is not surprising as higher energy leads to a more "chaotic" statistical dissociation on the ground state surface over energy-favored $NH_2+H$ channel. Experimental quantum yield for $NH(a^1\Delta)$ at 193.3 nm is <0.008 in ref. [41], which in good agreement with our suggested value of < 0.0029% at 7.4 eV, taking into account the zero-point-energy correction (~1.0 eV at ground state minimum). Another noticeable observation from experiment is that no $NH(X^3\Sigma^-)$ is detected at wavelengths longer than 160 nm[41], while our simulations suggests a similar result with almost no $NH(X^3\Sigma^-)$ for total energy ≤7.8 eV. In fact, even at higher energy the ratio of $NH(X^3\Sigma^-)$ is still small. This observation will be analyzed below.

Table III. $NH(a^1\Delta, X^3\Sigma^-)$ quantum yields as a function of $E_0^{tot}$

| $E_0^{tot}$(eV) | M | $NH(a^1\Delta)+H_2$ | $NH(X^3\Sigma^-)+H_2$ |
|---|---|---|---|
| 7.4 | 2500 | 0.20% | 0.00% |
| | 5000 | 0.28% | 0.00% |
| | 7500 | 0.29% | 0.00% |
| 7.8 | 2500 | 0.56% | 0.00% |
| | 5000 | 0.44% | 0.02% |
| | 7500 | 0.45% | 0.01% |
| 8.2 | 2500 | 1.40% | 0.12% |
| | 5000 | 1.30% | 0.18% |
| | 7500 | 1.32% | 0.20% |
| 8.6 | 2500 | 2.44% | 0.24% |
| | 5000 | 2.42% | 0.22% |
| | 7500 | 2.40% | 0.21% |

Below in Figures. 4-6 we provide typical trajectories that represent different dissociation mechanisms. Animated versions of Figures. 4-6 with 3D moving molecules can be found in Supporting Information (SI). While a single trajectory is not statistically significant, representative trajectories provide chemically relevant information about the nuclear dynamics.

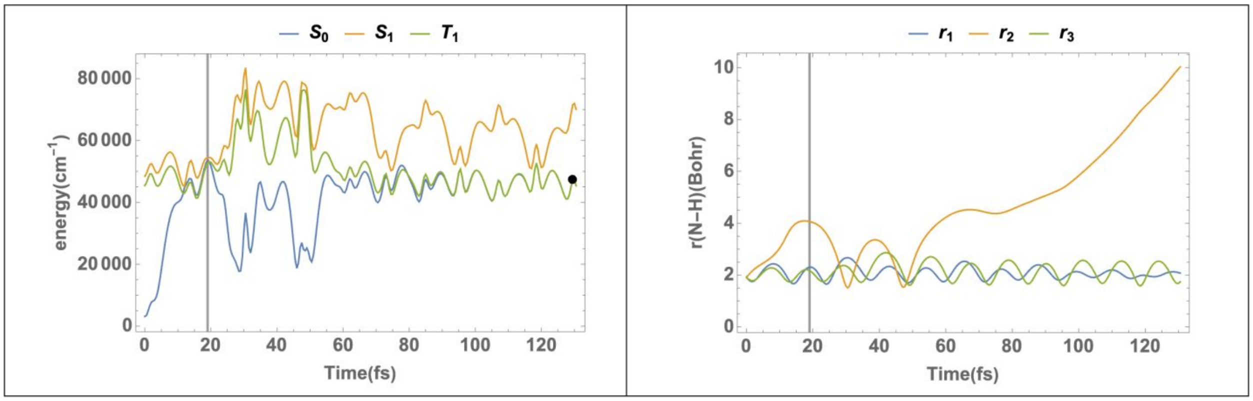

Figure 4. Indirect dissociation in the radical ($NH_2$(X)+H) channel. Left panel shows the electronic energies as a function of time. Right panel shows the three N-H bond distances $r_i = R(\text{N-H}^i)$, $i$= 1-3. $S_1$ to $S_0$ hop occurs at the vertical line. Dot indicates final state at asymptote.

Simple direct dissociation to $NH_2$+H refers to trajectories that go directly into the radical channel via internal conversion without revisiting the Franck-Condon region. Such a mechanism has been reported in previous work[47] and provides the preponderance of the product flux. Here in Figure 4 we show indirect dissociation into the radical channel. Indirect dissociation refers to molecules that internally convert to the ground state and then return to the Franck-Condon region from which they dissociate quasi-statistically. Molecules going through indirect dissociation with high internal energy can exit through multiple dissociation pathways. Here the $NH_2$+H channel is only one of them. The limited yield of the molecular channel is consistent with *ab initio* calculations which suggests a high barrier in the molecular channel compared with radical channel, even though the former is energetically more favored (see Figure 2). Note that in the $NH_2$+H channel, the triplet $T_1$ plays a silent role because $T_1$ and $S_0$ both correlate with the $NH_2(X^2B_1)$ product.

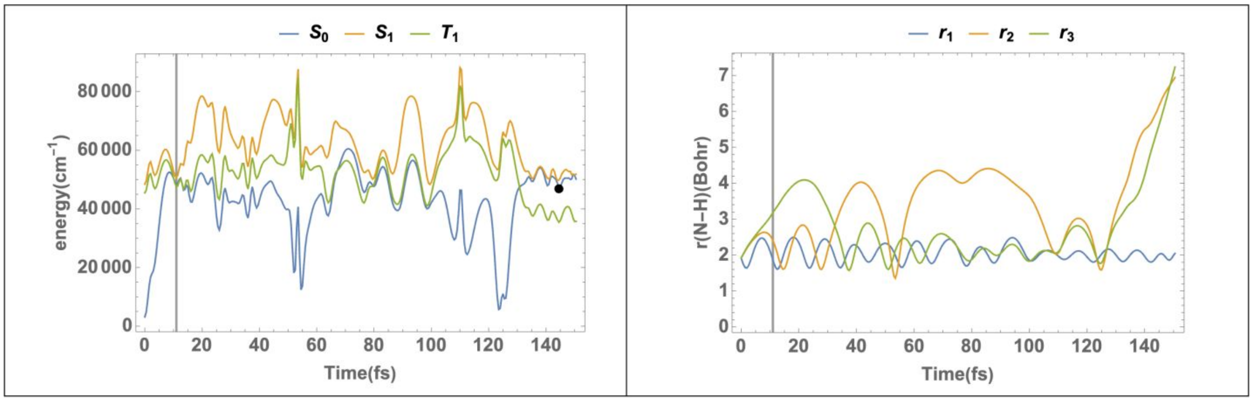

Figure 5. Production of NH($a^1\Delta$). Left panel shows the electronic energies as a function of time. Right panel shows the three N-H bond distances $r_i$ = $R$(N-H$^i$), $i$= 1-3. $S_1$ to $S_0$ hop occurs at the vertical line. Dot indicates final state at asymptote.

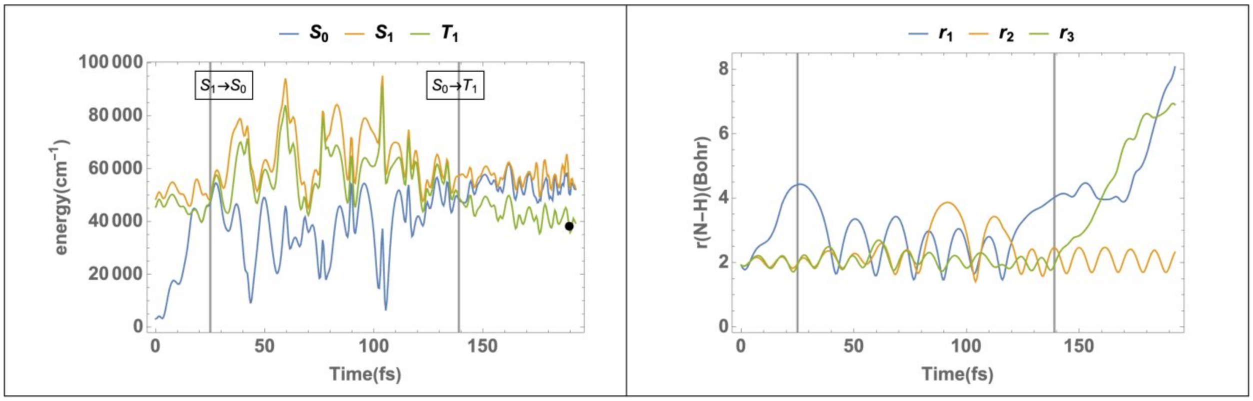

Figure 6. Production of NH($X^3\Sigma^-$). Left panel shows the electronic energies as a function of time. Right panel shows the three N-H bond distances $r_i$ = $R$(N-H$^i$), $i$= 1-3. Hops occur at the vertical lines. Dot indicates final state at asymptote.

Figures 5 and 6 show typical trajectories for the production of NH($a^1\Delta$, $X^3\Sigma^-$), respectively. The production of NH($a^1\Delta$) is more favorable than that of NH($X^3\Sigma^-$) as the former is spin-allowed. In order to produce NH($X^3\Sigma$), the molecule travelling on the ground singlet state surface will need to hop near a $S_0/T_1$ crossing. Although the effective SOC in such a region is small (<20 cm$^{-1}$), the molecule can ev\entually accumulate enough probability when oscillating around this intermediate region. The trajectory in Figure 6 illustrates and confirms this hypothesis. The molecule forms intermediates between 130-150 fs where the energies of $S_0$ and $T_1$ are close (energy difference < 2000 $cm^{-1}$) and the intersystem crossing happens. Most trajectories still dissociate on $S_0$ and it is quite rare for such hop to happen. In fact, for 10000 trajectories, only ~1.8% percent ended up with the $NH+H_2$ channel, and 0.2% produce $NH(X^3\Sigma^-)$. Given the small probability of such hop, this characterization of the intersystem crossing in $NH_3$ dissociation is more of a qualitative analysis instead of a quantitative one. One reason for the small probability of intersystem crossing is the relatively small SOC in light elements. We anticipate more significant results when we apply our methods to systems with larger SOC.

It should be pointed out that the detection of $NH(X^3\Sigma^-)$ in experiment does not necessarily mean that an intersystem crossing has happened, when higher energies are involved. A migration from a higher triplet state such as $A^3\Pi$ is possible. The $NH(X^3\Sigma)$ + (H+H) ($^3\Sigma$) channel will also need to be taken into consideration when, at higher energies, the $H_2$ can become highly stretched.[34] However, these channels require much higher excitation energies or pumping up to higher excited states than $S_1$. Since our simulation is conducted with very limited excitation energies above the minimum of $S_1$, it is safe to assume the $NH(X^3\Sigma)$ is a signature of intersystem crossing..

## IV. Summary and conclusions

Using recently reported potential energy surfaces and SOC surfaces of the first two singlets and one triplet of $NH_3$, we perform semi-classical trajectory simulations with the SHARC suite of nonadiabatic dynamics codes to investigate the molecular dissociation channel in $NH_3$. A total of ~40,000 trajectories were calculated to obtain convincing statistical $NH(a^1\Delta, X^3\Sigma^-)+H_2$ percent distributions in the molecular channel, in good agreement with the available experimental results. We found that the production of $NH+H_2$ is not direct but is only achieved through a quasi-statistical dissociation mechanism after internal conversion to its ground electronic state. Moreover, intersystem crossing was found along the $NH+H_2$ channel though the SOC is small. The ability to perform large batches of trajectories with

PESs and SOC surfaces enables the detection of intersystem crossing, which is a rare event. Our methods of fitting SOC surfaces in nonadiabatic system allows for study of competing intersystem crossing and internal conversion, providing an alternative to on-the-fly methods with higher efficiency and accuracy. Future work will focus on applying the method to nonadiabatic systems with more significant SOC and performing quantum dynamics to further understand the competing reaction mechanisms. The fit SOC surfaces provides adiabatic SOC matrix at almost no additional cost, which can also be used to study the geometric phase and spin-polarization effect[60, 61] with accurate nonadiabatic dynamics methods.

## SUPPORTING INFORMATION

Movies for the reported trajectories in Figures 4-6 can be obtained as Supporting Information.

## ACKNOWLEDGMENTS

This work was supported by National Science Foundation grant (CHE-1954723 to D.R.Y.) and Department of Energy grant (DE-SC0015997 to H. G.). The authors are grateful for a generous grant of computer time on the Maryland Advanced Research Computing Center. The SHARC program used in this work was obtained from sharc-md.org.

## NOTES

The authors declare no competing financial interest.

## ORCID

Yuchen Wang: 0000-0003-0479-3776

Hua Guo: 0000-0001-9901-053X

David R. Yarkony: 0000-0002-5446-1350

References:

1. M. Born and R. Oppenheimer, *Ann. Phys.*, 1927, **84**, 0457.
2. D. R. Yarkony, *Rev. Mod. Phys.*, 1996, **68**, 985.
3. W. Domcke, D. R. Yarkony and H. Köppel, *Conical Intersections: Electronic Structure, Dynamics and Spectroscopy*, World Scientific, Singapore, 2004.
4. B. F. E. Curchod and T. J. Martínez, *Chem. Rev.*, 2018, **118**, 3305-3336.
5. B. G. Levine and T. J. Martínez, *Annu. Rev. Phys. Chem.*, 2007, **58**, 613-634.
6. D. A. Fedorov, S. Seritan, B. S. Fales, T. J. Martínez and B. G. Levine, *J. Chem. Theory Comput.*, 2020, **16**, 5485.
7. S. Mai, P. Marquetand and L. González, *WIREs: Comput. Mol. Sci.*, 2018, **8**, e1370.
8. H. Guo and D. R. Yarkony, *Phys. Chem. Chem. Phys.*, 2016, **18**, 26335.
9. Y. Guan, C. Xie, D. R. Yarkony and H. Guo, *Phys. Chem. Chem. Phys.*, 2021, **23**, 24962.
10. L. Zhang, Y. Shu, S. Sun and D. G. Truhlar, *J. Chem. Phys.*, 2021, **154**, 094310.
11. N. Ananth, *Annu. Rev. Phys. Chem.*, 2022, **73**, 14.11.
12. J. Westermayr and P. Marquetand, *Chem. Rev.*, 2021, **121**, 9873.
13. Y. Shu, Z. Varga, S. Kanchanakungwankul, L. Zhang and D. G. Truhlar, *J. Phys. Chem. A*, 2022, **126**, 992–1018.
14. M. Richter, P. Marquetand, J. González-Vázquez, I. Sola and L. González, *J. Chem. Theory Comput.*, 2011, **7**, 1253.
15. C. M. Marian, *WIREs: Comput. Mol. Sci.*, 2012, **2**, 187.
16. C. M. Marian, *Annu. Rev. Phys. Chem.*, 2021, **72**, 617.
17. F. Fritsch, T. Weike and W. Eisfeld, *J. Chem. Phys.*, 2022, **156**, 054115.
18. B. F. E. Curchod, C. Rauer, P. Marquetand, L. González and T. J. Martínez, *J. Chem. Phys.*, 2016, **144**, 101102.
19. S. Mukherjee, D. A. Fedorov and S. A. Varganov, *Annu. Rev. Phys. Chem.*, 2021, **72**, 515.
20. J. Westermayr, M. Gastegger and P. Marquetand, *J. Phys. Chem. Lett.*, 2020, **11**, 3828.
21. S. Mukherjee and S. A. Varganov, *J. Chem. Phys.*, 2021, **155**, 174107.
22. A. O. Lykhin, D. G. Truhlar and L. Gagliardi, *J. Am. Chem. Soc.*, 2021, **143**, 5878.
23. F. An, J. Chen, X. Hu, H. Guo and D. Xie, *J. Phys. Chem. Lett.*, 2020, **11**, 4768.
24. T. Lenzen, W. Eisfeld and U. Manthe, *J. Chem. Phys.*, 2019, **150**, 244115.
25. Y. Wang, Y. Guan, H. Guo and D. R. Yarkony, *J. Chem. Phys.*, 2021, **154**, 094121.
26. B. M. Weight, A. Mandal and P. Huo, *J. Chem. Phys.*, 2021, **155**, 084106.
27. J. M. Bowman, B. J. Braams, S. Carter, C. Chen, G. Czakó, B. Fu, X. Huang, E. Kamarchik, A. R. Sharma, B. C. Shepler, Y. Wang and Z. Xie, *J. Phys. Chem. Lett.*, 2010, **1**, 1866-1874.
28. B. Zhao, S. Han, C. L. Malbon, U. Manthe, D. Yarkony and H. Guo, *Nat. Chem.*, 2021, **13**, 909.
29. Y. Guan, H. Guo and D. R. Yarkony, *J. Chem. Theory Comput.*, 2019, **16**, 302.
30. Y. Guan and D. R. Yarkony, *J. Phys. Chem. Lett.*, 2020, **11**, 1848.
31. H. Okabe and M. Lenzi, *J. Chem. Phys.*, 1967, **47**, 5241.
32. M. Suto and L. Lee, *J. Chem. Phys.*, 1983, **78**, 4515.
33. V. Vaida, W. Hess and J. L. Roebber, *J. Phys. Chem.*, 1984, **88**, 3397-3400.

34. U. Mänz, E.-A. Reinsch, P. Rosmus, H.-J. Werner and S. V. O'Neil, *J. Chem. Soc. Faraday Trans.*, 1991, **87**, 1809-1814.
35. M. I. McCarthy, P. Rosmus, H.-J. Werner, P. Botschwina and V. Vaida, *J. Chem. Phys.*, 1987, **86**, 6693-6700.
36. D. H. Mordaunt, M. N. R. Ashfold and R. N. Dixon, *J. Chem. Phys.*, 1996, **104**, 6460-6471.
37. V. Vaida, M. I. McCarthy, P. C. Engelking, P. Rosmus, H.-J. Werner and P. Botschwina, *J. Chem. Phys.*, 1987, **86**, 6669-6676.
38. A. Bach, J. M. Hutchison, R. J. Holiday and F. F. Crim, *J. Chem. Phys.*, 2002, **116**, 4955.
39. W. Lai, S. Y. Lin, D. Xie and H. Guo, *J. Chem. Phys.*, 2008, **129**, 154311.
40. Z. H. Li, R. Valero and D. G. Truhlar, *Theo. Chem. Acc.*, 2007, **118**, 9-24.
41. R. D. Kenner, F. Rohrer and F. Stuhl, *J. Chem. Phys.*, 1987, **86**, 2036-2043.
42. J. Biesner, L. Schnieder, J. Schmeer, G. Ahlers, X. Xie, K. H. Welge, M. N. R. Ashfold and R. N. Dixon, *J. Chem. Phys.*, 1988, **88**, 3607-3616.
43. J. Biesner, L. Schnieder, G. Ahlers, X. Xie, K. H. Welge, M. N. R. Ashfold and R. N. Dixon, *J. Chem. Phys.*, 1989, **91**, 2901-2911.
44. D. Bonhommeau and D. G. Truhlar, *J. Chem. Phys.*, 2008, **129**, 014302.
45. D. Bonhommeau, R. Valero, D. G. Truhlar and A. W. Jasper, *J. Chem. Phys.*, 2009, **130**, 234303.
46. J. Ma, X. Zhu, H. Guo and D. R. Yarkony, *J. Chem. Phys.*, 2012, **137**, 22A541.
47. J. Ma, C. Xie, X. Zhu, D. R. Yarkony, D. Xie and H. Guo, *J. Phys. Chem. A*, 2014, **118**, 11926-11934.
48. C. Xie, J. Ma, X. Zhu, D. H. Zhang, D. R. Yarkony, D. Xie and H. Guo, *J. Phys. Chem. Lett.*, 2014, **5**, 1055-1060.
49. C. Xie, X. Zhu, J. Ma, D. R. Yarkony, D. Xie and H. Guo, *J. Chem. Phys.*, 2015, **142**, 091101.
50. K. Giri, E. Chapman, C. S. Sanz and G. Worth, *J. Chem. Phys.*, 2011, **135**, 044311.
51. X. Zhu and D. R. Yarkony, *J. Chem. Phys.*, 2010, **132**, 104101.
52. D. R. Yarkony, *Int. Rev. Phys. Chem.*, 1992, **11**, 195-242.
53. D. G. Fedorov and M. S. Gordon, in *Low-Lying Potential Energy Surfaces*, ACS Publications, 2002, ch. 13, pp. 276-297.
54. R. McWeeny, *J. Chem. Phys.*, 1965, **42**, 1717.
55. G. Granucci, M. Persico and G. Spighi, *J. Chem. Phys.*, 2012, **137**, 22A501.
56. H. Lischka, T. Müller, P. G. Szalay, I. Shavitt, R. M. Pitzer and R. Shepard, *WIRS: Comput. Mol. Sci.*, 2011, **1**, 191-199.
57. H. Lischka, R. Shepard, R. M. Pitzer, I. Shavitt, M. Dallos, T. Müller, P. G. Szalay, M. Seth, G. S. Kedziora and S. Yabushita, *Phys. Chem. Chem. Phys.*, 2001, **3**, 664.
58. R. B. Gerber, M. A. Ratner and V. Buch, *Chem. Phys. Lett.*, 1982, **91**, 173.
59. R. D. Coalson, *Chem. Phys. Lett.*, 1990, **165**, 443.
60. Y. Wang and D. R. Yarkony, *J. Chem. Phys.*, 2021, **155**, 174115.
61. X. Bian, Y. Wu, H.-H. Teh, Z. Zhou, H.-T. Chen and J. E. Subotnik, *J. Chem. Phys.*, 2021, **154**, 110901.